

Contents lists available at ScienceDirect

## International Journal of Plasticity

journal homepage: www.elsevier.com/locate/ijplas





# Plastic flow behaviors of high-strength dual-phase Ni-SiOC nanocomposites

Bingqiang Wei<sup>a</sup>, Wenqian Wu<sup>a</sup>, Michael Nastasi<sup>b</sup>, Lin Li<sup>c</sup>, Jian Wang<sup>a,\*</sup>

- <sup>a</sup> Mechanical & Materials Engineering, University of Nebraska-Lincoln, Lincoln, NE 68588, USA
- <sup>b</sup> Department of Nuclear Engineering, Texas A&M University, College Station, TX 77843, USA
- <sup>c</sup> Metallurgical and Materials Engineering, The University of Alabama, Tuscaloosa, AL 35487, USA

#### ARTICLE INFO

#### Keywords: Strength Plasticity Microstructure Crystal-amorphous nanocomposite

#### ABSTRACT

High-strength materials with good plastic flow stability are highly desirable for structural applications. Refining grain size can effectively enhance flow strength but often cause plastic flow instability. Here, we demonstrated that nanosized amorphous ceramics SiOC impart a simultaneous enhancement of strength and plastic flow stability to Ni-based nanocomposites. The cosputtered Ni-SiOC nanocomposites exhibit core (crystalline Ni)-shell (amorphous SiOC) nanostructures and develop nanograined Ni composite containing amorphous ceramic SiOC nanoparticles during annealing up to 800 °C. Corresponding to the developed microstructures, in-situ scanning electron microscope (SEM) micropillar compression tests at deformation temperatures range from room temperature (RT) to 400°C reveal that the core-shell nanostructure shows high strength of 2.5 GPa at RT and 1.6 GPa at 400 °C with compressive strain up to 40%, while the nanograined Ni composite containing amorphous ceramic nanoparticles exhibits high strength of 3.0 GPa at RT and 2.0 GPa at 400 °C with compressive strain up to 50%. Most intriguingly, both nanocomposites do not exhibit obvious strain hardening/softening behavior during compression up to 50%. The high strain rate sensitivity (0.02 at RT to 0.05 at 400  $^{\circ}$ C) and the small activation volume (8b<sup>3</sup> at RT to 10b<sup>3</sup> at 400 °C) that were measured based on strain rate jump tests suggest dislocation slips as dominant deformation mechanisms in Ni grains, which is further evidenced by microscopy. Superb plastic flow stability is attributed to microstructure-promoted plastic codeformation between amorphous ceramics and Ni grains as confirmed by microstructure characterizations. Moreover, amorphous ceramic SiOC inhibit grain coarsening of Ni, preventing deformation induced softening.

## 1. Introduction

Advanced metallic materials with ultrahigh strength, large plasticity and good thermal stability are highly desirable for the applications under high temperature and irradiation environments. Such desired properties could be realized in materials with characteristic microstructure. For example, high density, thermally stable interfaces play crucial role in strengthening materials and improving irradiation tolerance as demonstrated in nanostructured laminates (Beyerlein et al., 2013; Chen et al., 2020; Wang et al., 2017; Xiao et al., 2015; Zhang et al., 2018). For ultra-fine and nano-grained materials, grain coarsening happens at high temperatures

Corresponding author. E-mail address: jianwang@unl.edu (J. Wang).

and/or irradiation, weakening materials (Liu et al., 2014; Meyers et al., 2006; Sharma et al., 2013; Wang et al., 2012). Retaining the microstructure in high temperature and irradiation environments could be realized through forming amorphous grain boundaries and/or secondary phases along grain boundaries (Freund et al., 2018; Grigorian and Rupert, 2019; Jiang et al., 2018; Schuler et al., 2020; Su et al., 2019; Zhang et al., 2017). Second phase strengthening is widely observed in metallic materials, for example, Ni-based superalloy with intermetallic compounds (Long et al., 2018; Reed, 2008). However, intermetallic compounds are intrinsically brittle at RT (Wang et al., 2022) and may decompose at elevated temperatures (Cao et al., 2021; Chyrkin et al., 2015; Jiang et al., 2019; Xiang et al., 2019). Moreover, their significant difference in elasticity and plasticity to the matrix leads to deformation incompatibility between secondary phase and matrix. Correspondingly, cracks usually tend to be initiated in secondary phase or at interfaces, especially under cyclic loading or high strain rate (Liu et al., 2018a; Ma et al., 2016). Therefore, it is desired to promote plastic co-deformation between secondary phase and matrix, for example by reducing the size of secondary phases to form coherent interfaces, such as the coherent nanosized L12 or  $\gamma$  phases in Ni-based superalloy and multi-principal element alloys (Fan et al., 2020; Grant et al., 2012; Han et al., 2021; He et al., 2016; Kim et al., 2015; Wang et al., 2020).

In contrast to intermetallic compounds, amorphous solids such as metallic glass and amorphous ceramics exhibit plastic flow ability especially when their featured size was reduced into nanoscale (Guo et al., 2007; Jang and Greer, 2010; Ming et al., 2020; Wei et al., 2021; Wu et al., 2019). In addition to refinement of the characteristic dimension, improving the plasticity of amorphous materials, especially preventing plastic flow instability, can be realized through microstructural engineering (Abdolrahim et al., 2013; Barai and Weng, 2009; Lieou et al., 2017). Crystalline-amorphous and amorphous-amorphous multilayers exhibit either uniform deformation or discrete shear bands, which depends on the thickness of individual layers and the type of interfaces between layers (Tran, 2021; Wang et al., 2017; Wang et al., 2007). Plastic deformation in metal-amorphous laminates is mainly accommodated by plastic deformation in metallic layers. Amorphous materials lack strain hardening ability, resulting in limited elongation after the elastic-strain region. Beyond the elastic limit, amorphous materials deform via shear transformation zones and fail by localized shear bands (Cui et al., 2016; Guo et al., 2014; Zhang et al., 2012). In addition to laminar microstructure, another approach to preventing plastic flow localization is to combine materials with distinct flow localization behaviors in a single composite composed of crystalline/amorphous phases (Liu et al., 2018b; Ming et al., 2022; Qiao et al., 2016; Zhou et al., 2013), and gradient or bimodal microstructures (Hasan et al., 2019; Ning et al., 2013; Shi et al., 2022; Tang et al., 2022; Yuan et al., 2019; Zhu et al., 2021). When deformed, such composites develop limited regions of flow localization. However, the alternation of flow localizing and uniformly deforming phases in the composite impedes individual flow-localized zones from extending across the entire length of material. Meanwhile, small, flow-localized zones are forced to re-nucleate throughout the microstructure without percolating.

Therefore, it is speculated that nanosized amorphous solids can impart a simultaneous enhancement of strength and plastic flow stability to amorphous reinforced metallic alloys. Here, we demonstrated this hypothesis with crystal-amorphous Ni-SiOC nanocomposites. Ni was chosen in this study because Ni-based alloys are important high temperature materials (Reed, 2008). Amorphous SiOC ceramic is chosen because it exhibits superior thermo-mechanical properties (strength and hardness, creep and oxidation) and structural stability at elevated temperatures (>1300 °C) and under irradiation (Su et al., 2017; Wang et al., 2001; Zhao et al., 2019). In this work, Ni-SiOC nanocomposites were synthesized through co-sputtering 75 at.%-Ni and 25 at.%-SiOC, and further tempered at different temperatures (400 °C, 600 °C and 800 °C) to modify the microstructure. The co-sputtered Ni-SiOC nanocomposites exhibit core (crystalline Ni)-shell (amorphous SiOC) nanostructures and develop nanograined Ni containing amorphous ceramic SiOC nanoparticles during annealing up to 800 °C. *In-situ* SEM micropillar compression tests revealed that Ni-SiOC nanocomposites exhibit high strengths, superb plastic flow stability, and no hardening/softening over a wide range of deformation temperatures. Such superb mechanical properties are attributed to microstructure-promoted plastic co-deformation between amorphous ceramics and Ni grains. Amorphous ceramic SiOC imparts high thermal stability to Ni-SiOC nanocomposites, inhibiting grain coarsening of Ni and retaining high strength at high temperature.

## 2. Experimental methods

Fig. 1 show the schematic diagram of the procedure for sample preparation, high temperature annealing and in-situ mechanical test.

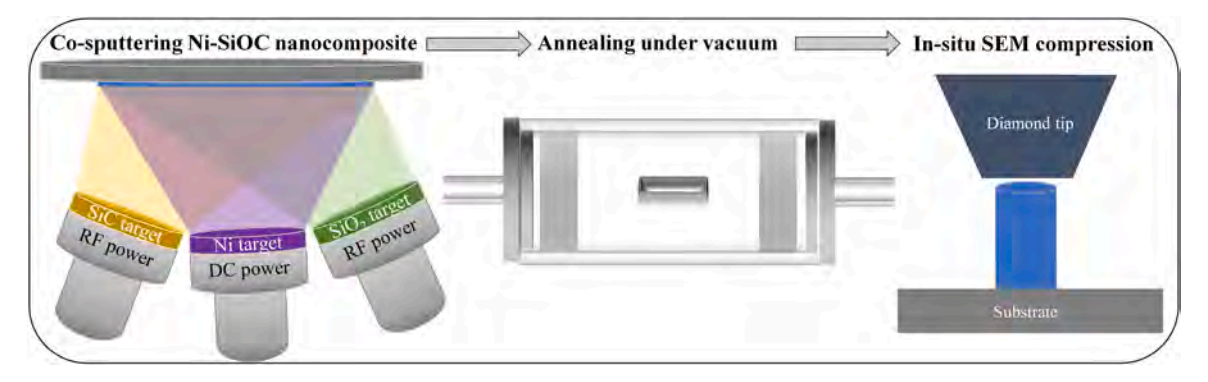
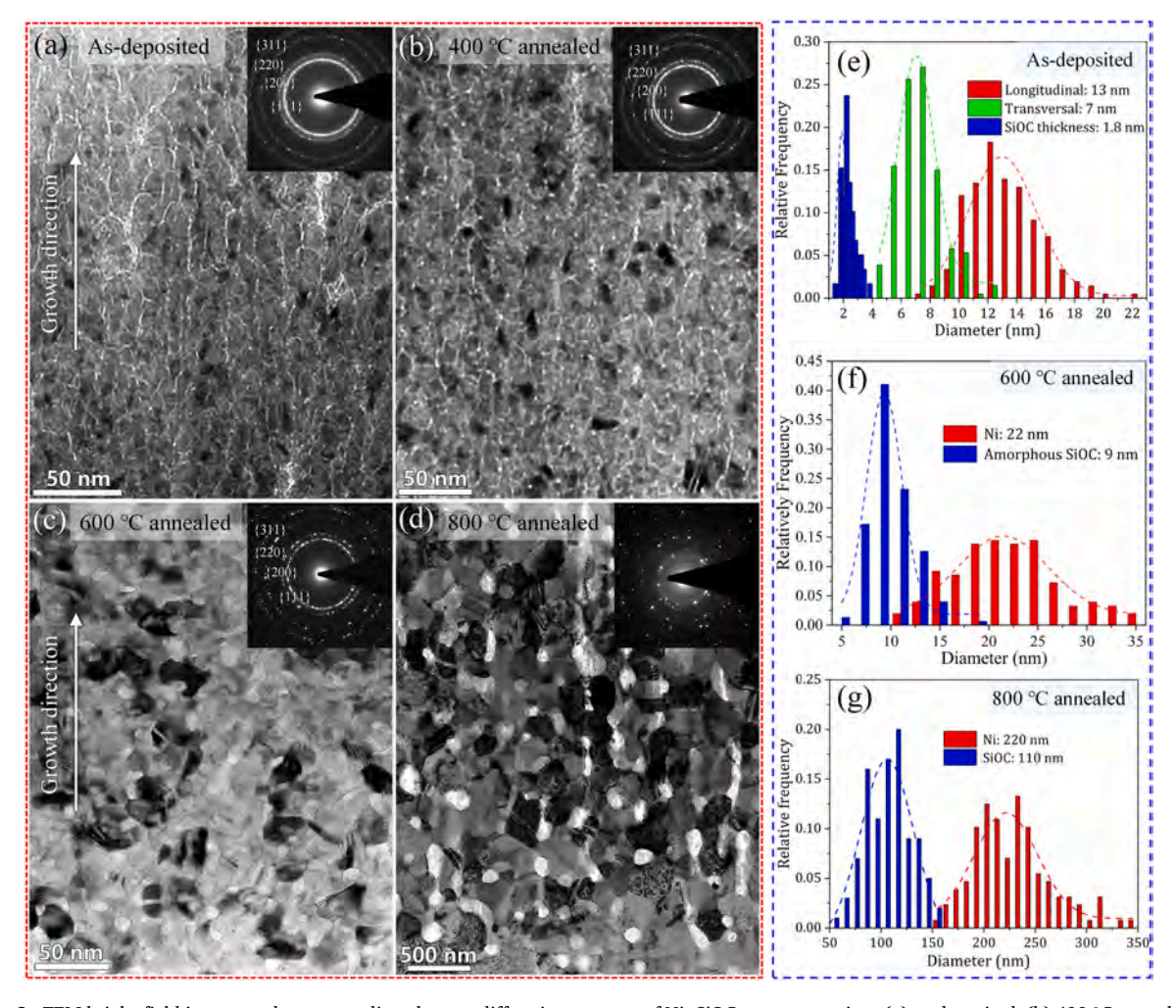


Fig. 1. Schematic diagram of the procedure for sample preparation, high temperature annealing and in-situ mechanical test.

The Ni-SiOC nanocomposite was synthesized by co-sputtering Ni (99.995%), SiC (99.5%) and SiO<sub>2</sub> (99.995%) targets onto a Si/SiO<sub>2</sub> substrate in an AJA ATC-2000F sputtering system with a base pressure of  $\sim 9.8 \times 10^{-6}$  Pa. Ar pressure was kept at 0.65 Pa during sputtering. The nominal composition is determined to be 74.4 at.% Ni, 5.6 at.% Si, 13.4 at.% O, and 6.6 at.% C (Wei et al., 2021) by energy dispersive X-ray spectroscopy analysis in transmission electron microscope (TEM) equipped with a quad Super-X detector. The as-deposited Ni-SiOC nanocomposite was then annealed at temperatures of 400 °C, 600 °C and 800 °C at vacuum circumstance for 1 hour to tune their microstructures. Micropillars with diameter of about 2-3 µm and aspect ratio (height/diameter) of 2 were prepared by focused ion beam (FIB) in an FEI Helios Nanolab 660 dual beam system. Fabrication of the micropillar was performed via a series of concentric annular milling/polishing with progressively de-escalated currents. Great care was taken to minimize the taper angle by using low milling current (30 kV, 10-40 pA) which was supposed to exhibit high lateral resolution and small beam size (Liao, 2006). Top and bottom diameters of the micropillar were measured to calculate the taper angle, which was controlled to be smaller than 1.5°. Final milling voltage/current of 2 kV/23 pA was used to reduce surface damage by Ga ion beam. In-situ SEM micropillar compression testing was conducted over a range of temperatures from RT to 400 °C to measure mechanical properties of Ni-SiOC nanocomposites. These tests are performed using a Hysitron PI85 PicoIndenter under a displacement-control mode at strain rate range from  $10^{-3}$  s<sup>-1</sup> to  $4 \times 10^{-2} \, \mathrm{s}^{-1}$ . In-situ heating was realized by using the micro electro-mechanical system heater provided by Bruker company. Strain rate jump (SRJ) tests were also conducted over the same range of temperatures to study the strain rate sensitivity of Ni-SiOC nanocomposite. Two to three micropillars were prepared for each testing. True stress-strain curves were obtained by the Elastic modulus correction formula for a pillar (Lee et al., 2009). Elastic modulus was obtained by nanoindentation test by using a Hysitron TI950 nanoindenter with a diamond Berkovich tip. Reduced elastic modulus (Er) was used here which was obtained from force vs. penetration depth curves (Oliver and Pharr, 1992). The penetration depth was maintained less than 10% thickness of thin film to minimize the influence of substrate on the results. Considering the additional displacement from the substrate and diamond tip, the valid



**Fig. 2.** TEM bright-field images and corresponding electron diffraction patterns of Ni- SiOC nanocomposites: (a) as-deposited, (b) 400 °C annealed, (c) 600 °C annealed and (d) 800 °C annealed; Characteristic size distribution of Ni nanograins and amorphous ceramic SiOC in (e) as-deposited, (f) 600 °C annealed nanocomposites.

displacement of the pillar was corrected by using Sneddon equation (Sneddon, 1965):

$$u_{pillar} = u_{mea.} - \frac{1 - v_{dia.}^2}{E_{dia.}} \left(\frac{F}{d_t}\right) - \frac{1 - v_{Si}^2}{E_{Si}} \left(\frac{F}{d_b}\right)$$
 (1)

where  $u_{mea.}$  and F are the measured displacement and force, respectively. The subtracted two items stand for the displacement from the diamond indenter and Si substrate, respectively.  $d_t$  and  $d_b$  are the top and bottom diameters of the pillar, and E and e0 are the Elastic modulus and Poisson's ratio, respectively. The corrected displacement was well consistent with that measured from the e1 in the in-situ video of compression tests. TEM and scanning TEM (STEM) characterizations were performed using an FEI Tecnai Osiris TEM operated at 200 kV. Cross-sectional TEM samples before and after deformation were prepared by FIB lift-out technique. Plasma cleaning for 2 mins was conducted to remove surface pollution before TEM observation.

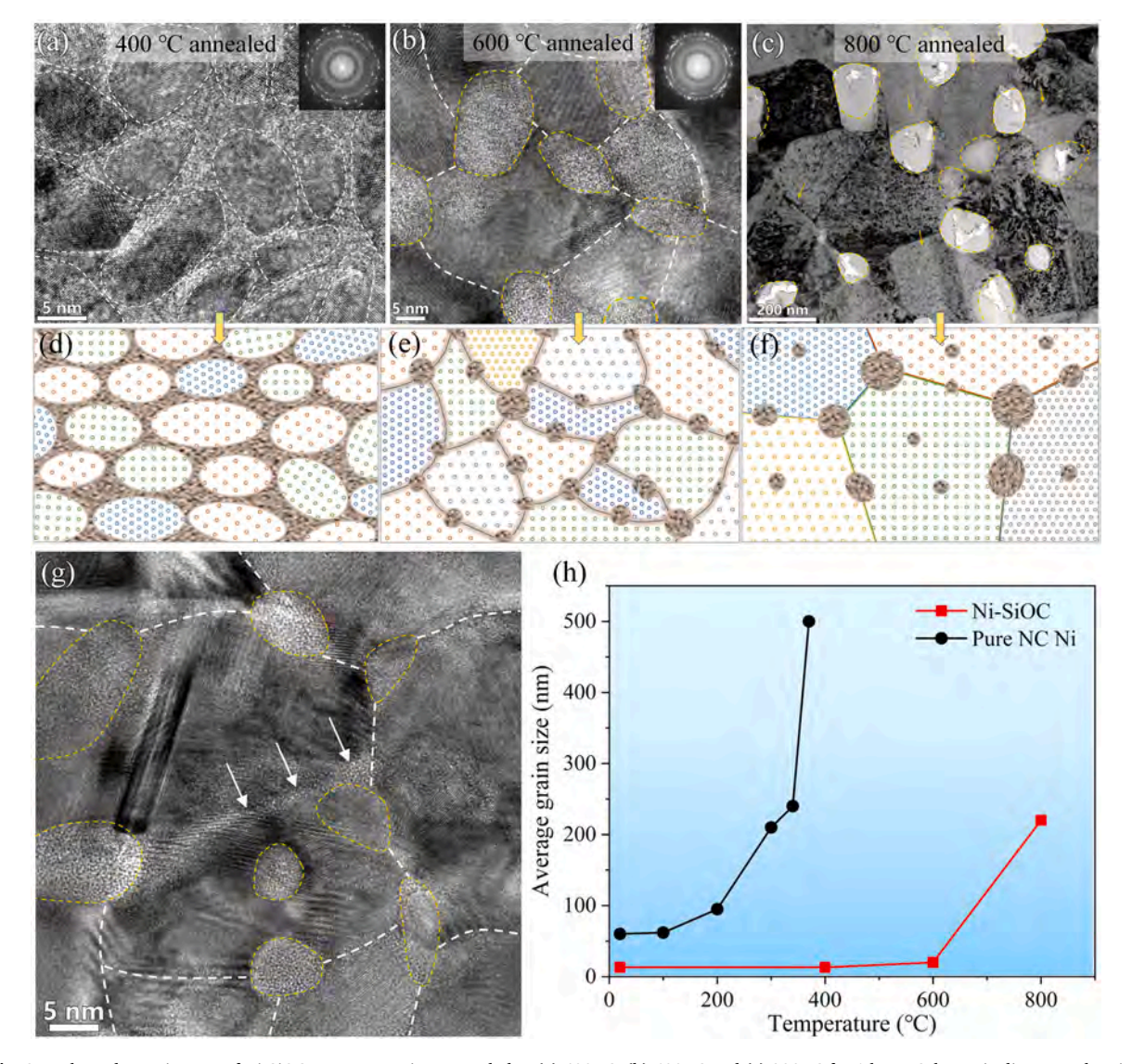


**Fig. 3.** Enlarged TEM images of Ni-SiOC nanocomposites annealed at (a) 400 °C, (b) 600 °C and (c) 800 °C for 1 hour; Schematic diagrams showing characteristic microstructures of (d) as-deposited and 400 °C annealed, (e) 600 °C and (f) 800 °C annealed nanocomposites; (g) HRTEM image of the 600 °C annealed Ni-SiOC nanocomposite with amorphous grain boundary; (h) Grain size coarsening process for Ni in Ni-SiOC nanocomposites and pure NC Ni.

#### 3. Results

#### 3.1. Characteristic microstructures of Ni-SiOC nanocomposites

Fig. 2 shows characteristic microstructures of Ni-SiOC nanocomposites. The as-deposited sample presents a core-shell nanostructure (Fig. 2a) which is composed of Ni nanograins (core) with elliptical shape along growth direction and amorphous SiOC grain boundaries (shell). The distributions of characteristic dimensions (Fig. 2e) show that the average size of Ni nanograins along longitudinal and transversal directions is  $\sim$ 13 nm and  $\sim$ 7 nm, respectively, and the average thickness of amorphous SiOC is  $\sim$ 1.8 nm. The diffraction rings in the corresponding diffraction pattern (inset in Fig. 2a) indicates random texture. The core-shell nanostructure remains stable up to 400°C as shown in Fig. 2b. No obvious growth of Ni nanograins was detected while the amorphous SiOC phase (bright contrast) tends to thicken at the triple junctions of Ni nanograins. After annealing at 600°C for 1 h, both crystalline Ni and amorphous SiOC grew up (Fig. 2c). In contrast to the quick and tremendous grain coarsening of nanocrystalline (NC) Ni during heating process (Sharma et al., 2012), the size of Ni grains in Ni-SiOC nanocomposites was still at nanoscale and no obvious texture developed as evidenced by the diffraction rings (inset in Fig. 2c), indicating good thermal stability of Ni-SiOC nanocomposites. This is attributed to the high thermal stability of amorphous ceramic SiOC and its strong pinning effect on Ni nanograins. Dark field imaging was used to measure the size distribution of Ni grains due to its relatively irregular shape and the overlap effect between nanograins. The average

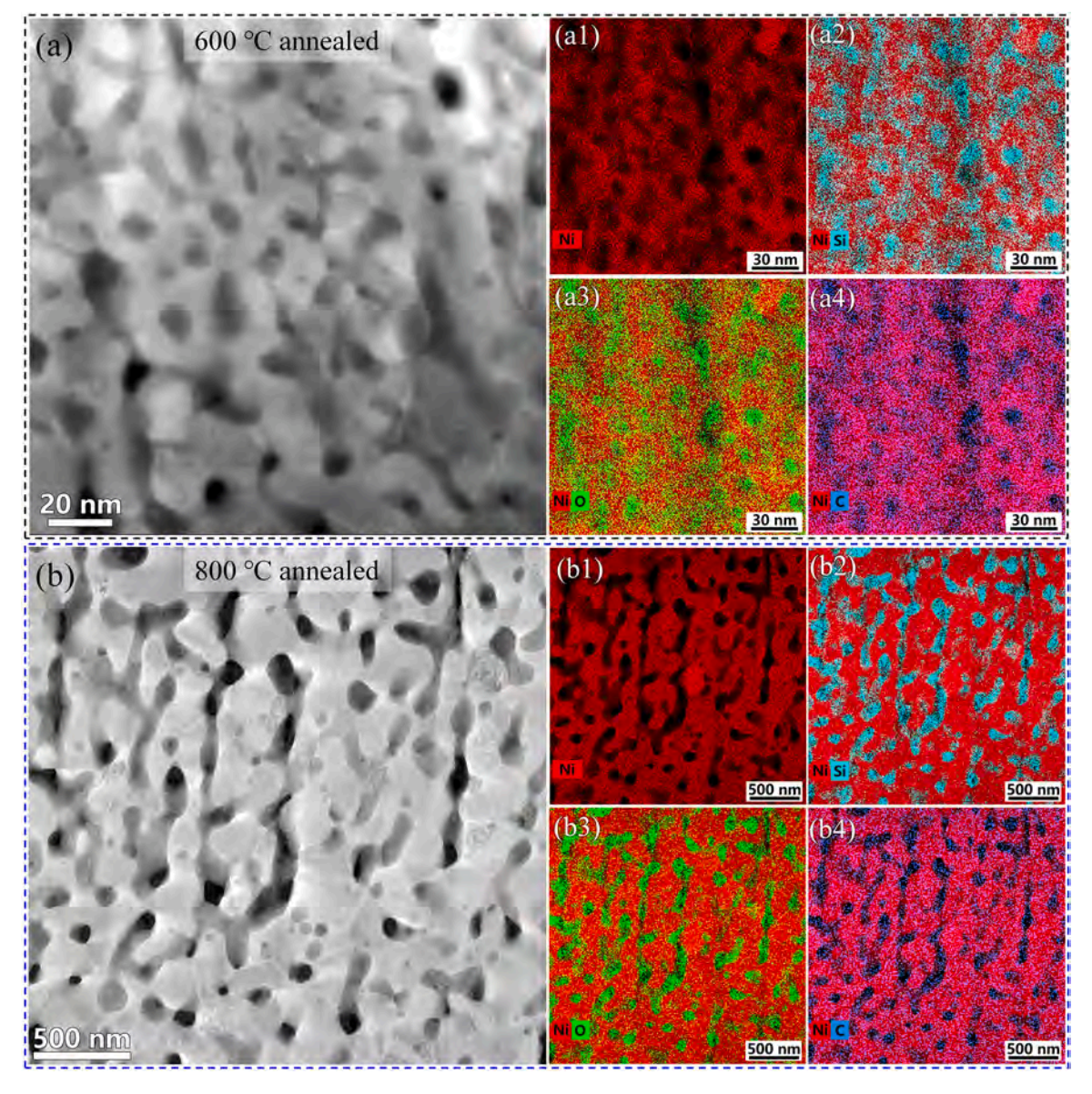


Fig. 4. STEM-Mapping of the (a) 600  $^{\circ}$ C and (b) 800  $^{\circ}$ C annealed Ni-SiOC nanocomposites.

diameter of Ni nanograins and SiOC particles are  $\sim$ 22 nm and  $\sim$ 9 nm (Fig. 2f), respectively. Fig. 2d shows a TEM bright-field image and corresponding diffraction pattern (inset) of 800 °C annealed sample. Ni grains and amorphous SiOC ceramic phase further grew up to  $\sim$ 220 nm and  $\sim$ 110 nm, respectively (Fig. 2g).

Fig. 3 presents microstructure evolution of the annealed Ni-SiOC nanocomposites. High-resolution TEM (HRTEM) image clearly shows the crystal-amorphous core-shell nanostructure of the 400 °C annealed sample (Fig. 3a). After annealed at 600 °C, the granular amorphous SiOC distributed both at grain boundaries and triple junctions of Ni nanograins (Fig. 3b), leading to the irregular shape of Ni nanograins. Moreover, amorphous SiOC phase was occasionally observed along grain boundaries as indicated by the white arrows in Fig. 3g. The amorphous halo and nanocrystal rings in the corresponding Fast Fourier Transformation (FFT) further verified the crystal-amorphous dual phase structure (insets in Fig. 3a and 3b). After annealed at 800 °C, amorphous SiOC particles were mainly distributed at the triple junctions of sub-micron sized Ni grains with near equiaxed shape (Fig. 3c). Smaller amorphous SiOC nanoparticles (10-30 nm) were also observed inside Ni grains as marked by yellow arrows in Fig. 3c. The corresponding schematic diagram of Ni-SiOC nanocomposites annealed at 400 °C, 600 °C and 800 °C are illustrated in Fig. 3d, f, respectively. Fig. 3h compares grain size coarsening process for Ni in Ni-SiOC nanocomposite and pure NC Ni (Sharma et al., 2012) during annealing. Obviously, the critical temperature for grain growth in our samples is much higher than that of pure NC Ni, proving high thermal stability of Ni-SiOC nanocomposites. The distribution of amorphous SiOC particles in 600 °C and 800 °C annealed samples were further verified by STEM-Mapping (Fig. 4). It is noted that Ni is distributed separately from Si, O and C amorphous elements, thus no intermetallic or compounds are produced after annealing. The interconnected feature of amorphous SiOC might be caused by the overlap effect.

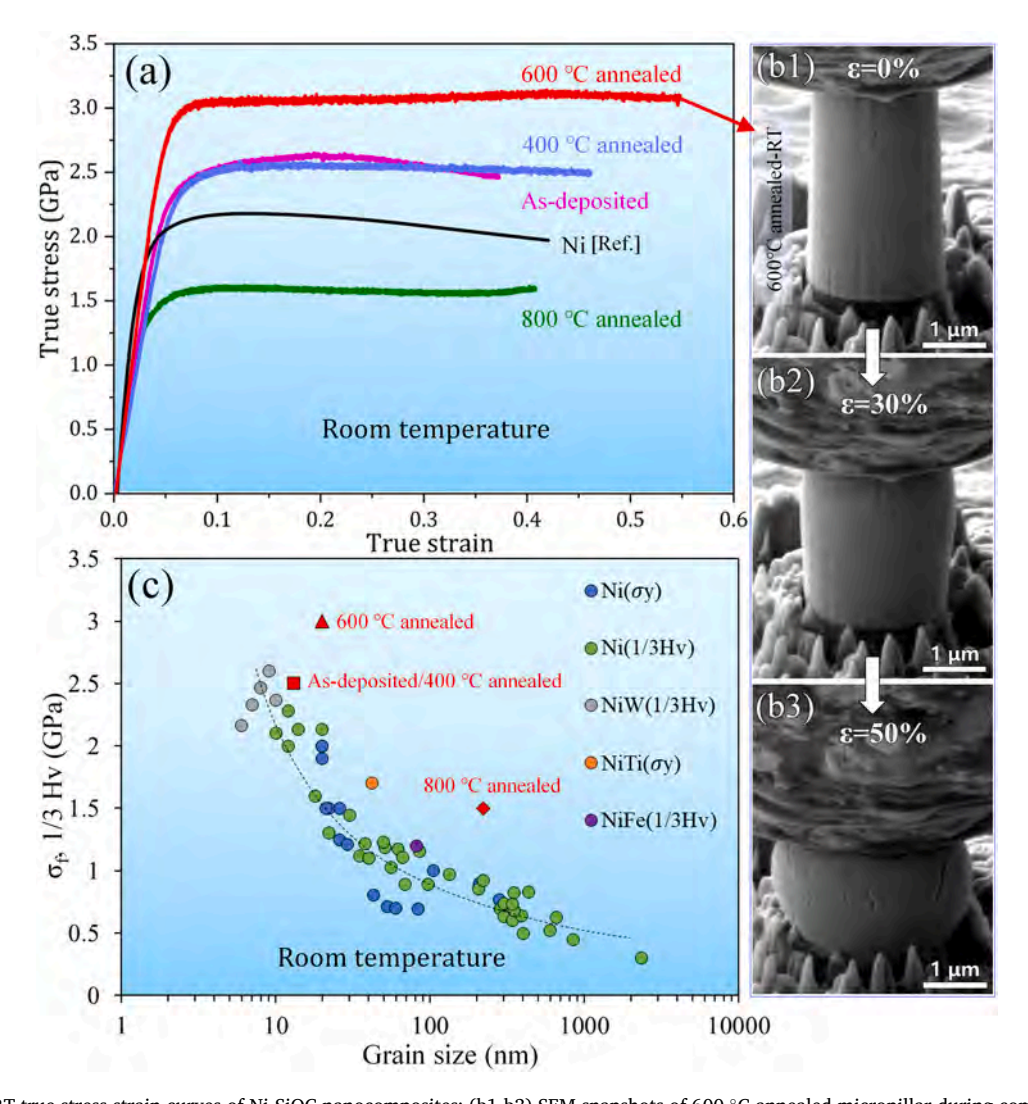


Fig. 5. (a) RT true stress-strain curves of Ni-SiOC nanocomposites; (b1-b3) SEM snapshots of 600 °C annealed micropillar during compression; (c) Comparison of RT flow strengths among Ni, Ni alloys and Ni-SiOC nanocomposites.

#### 3.2. High strength and plastic flow stability of Ni-SiOC nanocomposites

In-situ SEM micropillar compression tests were conducted at temperatures up to 400 °C with a constant strain rate of  $10^{-3}$  s<sup>-1</sup>. Fig. 5a shows the RT true stress-strain curves of Ni-SiOC nanocomposites at different states (as-deposited, 400 °C-, 600 °C- and 800 °Cannealed). The reported mechanical property of pure NC Ni with a grain size of 20 nm (Pan et al., 2007) was added for comparison. The as-deposited and 400 °C annealed Ni-SiOC nanocomposites with the similar core-shell structure exhibit the similar mechanical response, i.e., flow strength of 2.5 GPa, compressive strain up to ~40% and no obvious strain softening/hardening behavior. In contrast to pure NC Ni with lower flow strength (2.0 GPa) and deformation induced grain growth associated with strain softening behavior at later deformation stage (Pan et al., 2007), the excellent mechanical properties of the as-deposited and 400 °C annealed Ni-SiOC nanocomposites were attributed to the core-shell structure, where amorphous ceramic boundaries act as strong barriers and sinks for dislocations and co-deform with Ni nanograins (Wei et al., 2021). Interestingly, the 600 °C annealed Ni-SiOC nanocomposite show simultaneously improved flow strength (3.0 GPa) and compressive plasticity (>50%) despite of the increased size of Ni grains and amorphous ceramic phase after annealing. Moreover, the material exhibits high plastic flow stability without obvious strain softening/hardening behavior. Fig. 5b shows the corresponding SEM snapshots of a compressed micropillar. The micropillar present large deformability and no crack or shear instability were observed. After annealed at 800 °C, the flow strength of Ni-SiOC nanocomposite decreases to ~1.5 GPa corresponding to grain growth from 22 nm to 220 nm. It must be noted that the strength is much higher than NC Ni with the same grain size. SiOC particles experienced clear plastic deformation during compression test, which will be discussed later. Fig. 5c compares flow strengths of Ni-SiOC nanocomposites with those of reported Ni and Ni alloys (Ebrahimi et al., 1999; Lu, 2016; Schuh et al., 2003; Schuh et al., 2002; Zhang et al., 2011), showing that Ni-SiOC nanocomposites at different states have much higher strength than the reported Ni and Ni alloys with similar grain size.

Corresponding to the thermally stable microstructure, Fig. 6a shows the true stress-strain curves of the as-deposited (Wei et al., 2021) and 600 °C annealed Ni-SiOC nanocomposites at deformation temperatures of 200 °C, 300 °C and 400 °C, respectively. In contrast with substantial decrease of flow strength and strain softening of NC Ni at high temperatures (Sharma et al., 2013), the Ni-SiOC nanocomposites maintain high strength, 2.5 GPa at RT to 1.6 GPa at 400 °C for the as-deposited sample and 3 GPa at RT to 2 GPa at 400 °C for the 600 °C annealed sample. More importantly, all curves do not show obvious strain softening/hardening behavior. Compared to NC Ni, Sharma et al. (2012, 2013) reported a significant decrease in yield strength from ~703 MPa at RT to ~184 MPa at 300 °C, which is ascribed to obvious grain growth from 60 nm to 210 nm when the sample was annealed at 300 °C for 30 min. In addition, strain softening behavior occurred in NC Ni at the later deformation stage (Sharma et al., 2013, 2012). Fig. 6b shows the temperature dependent flow strength of Ni-SiOC nanocomposites and reported NC Ni (Sharma et al., 2013). Clearly, the Ni-SiOC nanocomposites exhibit much higher strength than pure Ni. In addition, Cottrell and Stokes (1955) pointed out that for a given microstructure the ratio of flow strengths at two temperatures reflects the ratio of thermal to athermal deformation components of the flow stress during straining. For a 200 K temperature change, the strength ratio is about 1.33 for Ni-SiOC nanocomposites and 1.2 for coarse grained Ni (Wang et al., 2006), implying a significant thermal deformation component in Ni-SiOC nanocomposites

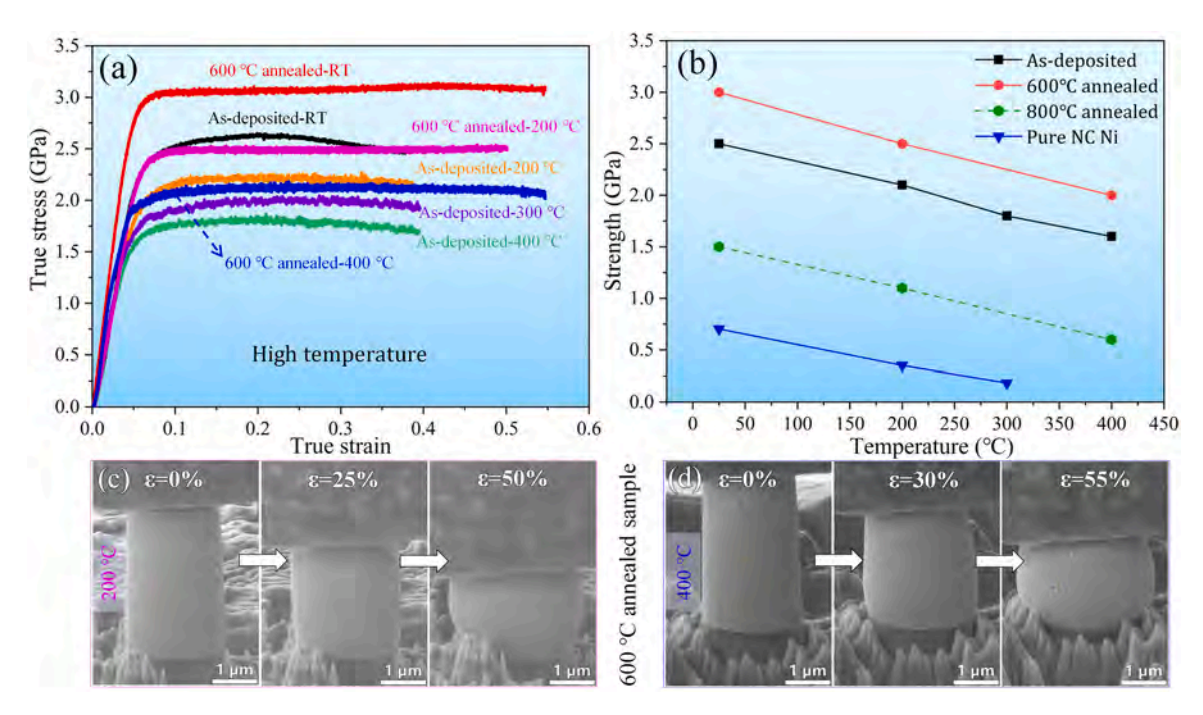


Fig. 6. (a) High temperature true stress-strain curves of as-deposited and 600 °C annealed Ni-SiOC nanocomposites; (b) Temperature-dependent strengths of NC Ni and Ni-SiOC nanocomposites; (c-d) SEM snapshots of 600 °C annealed micropillars deformed at 200 °C and 400 °C, respectively.

(Brandstetter et al., 2005; Wang and Ma, 2004), which will be discussed based on deformation mechanisms. Fig. 6c and 6d present the SEM snapshots of 600 °C annealed micropillars deformed at 200 °C and 400 °C, respectively, revealing high plastic flow stability.

#### 4. Discussion

#### 4.1. Deformation mechanisms of Ni nanograins

Plastic deformation in Ni nanograins is accommodated by dislocation slips. Since nucleation of dislocations from grain boundaries and crystal-amorphous interfaces in Ni nanograins are highly rate controlling deformation processes, we studied the temperature and strain rate dependence of the deformation behavior based on SRJ testing to understand the role of amorphous ceramics in deformation processes of Ni-SiOC nanocomposites. SRJ testing was conducted with a sequence of  $10^{-3}$  s<sup>-1</sup>  $\rightarrow 10^{-2}$  s<sup>-1</sup>  $\rightarrow 2 \times 10^{-3}$  s<sup>-1</sup>  $\rightarrow 2 \times 10^{-2}$  s<sup>-1</sup>  $\rightarrow 4 \times 10^{-3}$  s<sup>-1</sup>  $\rightarrow 2 \times 10^{-2}$  s<sup>-1</sup>  $\rightarrow 2 \times 10^{-3}$  s<sup>-1</sup>  $\rightarrow 10^{-2}$  s<sup>-1</sup>  $\rightarrow 10^{-3}$  s<sup>-1</sup> at different temperatures. Fig. 7a-c show the true stress-strain curves of 600 °C annealed samples and corresponding SEM snapshots of micropillars, which were conducted at RT, 200 °C and 400 °C, respectively. The flow stress increased with increasing strain rate, showing positive strain rate sensitivity. Also, the step height corresponding to the same strain rate increased with increasing temperature, indicating an increased strain rate sensitivity with temperature. Another important feature is the corresponding SEM snapshots of micropillars during SRJ tests (Fig. 7a1-c1) present high plastic flow stability with plastic strain up to 60%.

The value of strain rate sensitivity (m) and corresponding activation volume (V) at different temperatures were calculated based on the two equations (Dalla Torre et al., 2005):  $m = \left[\frac{d(\ln \sigma_f)}{d(\ln \hat{e})}\right]_T$  and  $V = \frac{\sqrt{3}kT}{m\sigma_f}$ , where  $\sigma_f$  indicates the flow strength,  $\dot{e}$  is the corresponding strain rate, k is the Boltzmann constant and T is the absolute temperature. The calculated values were presented in table 1, in which the values of m and V for the as-deposited Ni-SiOC with core-shell structures was also added for comparison. Based on the values of m and V, the mechanisms of Coble creep and grain boundary sliding that were proposed for NC metals when deforming at high temperature were ruled out, because of the much smaller value of m while higher value of V than that of grain boundary diffusion-mediated diffusional creep (m~1, V~1b<sup>3</sup>) and grain boundary sliding mechanism (m~0.5, V~1b<sup>3</sup>) (Wang et al., 2006), where b is the magnitude of a full Burgers vector in Ni. Correspondingly, the dominated deformation mechanism of Ni-SiOC nanocomposites must be related to dislocation motion in Ni nanograins, Fig. 8a, b show the temperature dependent strain rate sensitivity and activation volume for reported pure Ni (Wang et al., 2006) and Ni-SiOC nanocomposites. Both physical quantities of Ni-SiOC nanocomposites increase with deformation temperature. However, the activation volume in nano-grained pure Ni decreases with deformation temperature because of the dynamic grain growth and enhanced grain boundary motion at high temperature (Sheinerman and Bobyley, 2018; Wang et al., 2012). Thus, the increased activation volume with deformation temperature in Ni-SiOC nanocomposites implies that grain boundary motion is less likely activated within 400 °C corresponding to the strong pinning effect by amorphous ceramic SiOC. Note that the activation volume of NC Ni and Ni-SiOC nanocomposite are much smaller than that of traditional coarse-grained Ni (inset in Fig. 8b). This was proposed to be related to significant change of rate-controlling mechanism from conventional intersection of gliding dislocations with forest dislocations in coarse-grained Ni to dislocation nucleation or depinning/escaping from grain boundary in NC grains and crystal-amorphous interface in Ni-SiOC nanocomposite (Wang and Ma, 2004; Wei et al., 2021). The later deformation mechanism entailed much smaller activation length (Cheng et al., 2003). The energy barrier for emitting lattice dislocation from grain boundaries was proposed to be larger than that needed to merely form a jog during dislocation intersection, producing higher strength ratio with temperature change (Hirth, 1972; Wang and Ma, 2004).

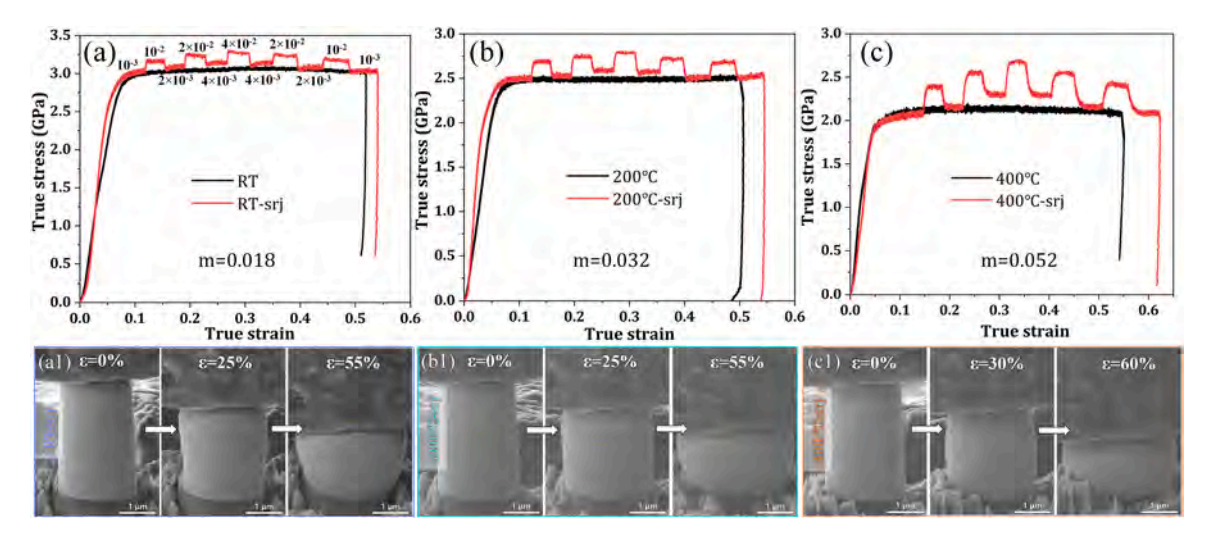


Fig. 7. (a-c) True stress-strain curves of SRJ tests of 600 °C annealed Ni-SiOC nanocomposite and corresponding SEM snapshots of micropillars at deformation temperatures of RT, 200 °C and 400 °C, respectively.

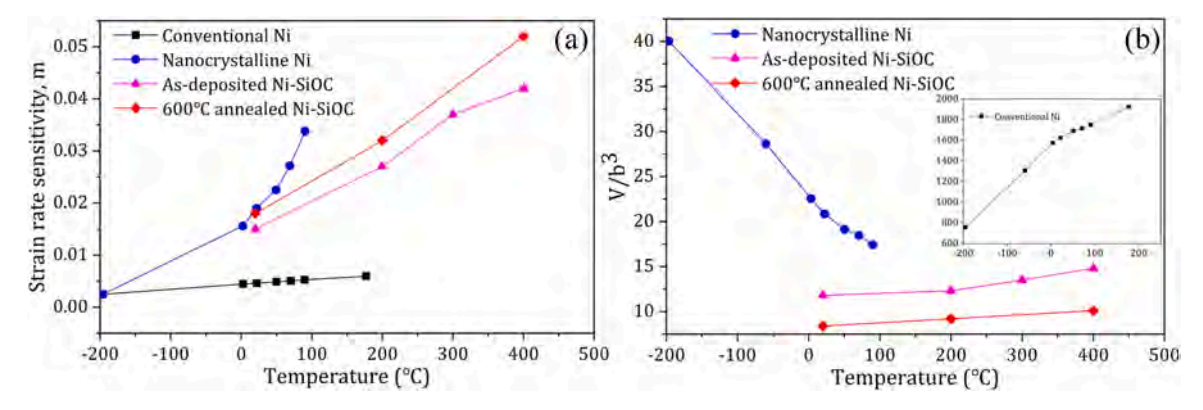


Fig. 8. (a) Comparison of strain rate sensitivity among Ni-SiOC nanocomposites, NC Ni and coarse-grained Ni at different temperatures; (b) Comparison of activation volume among Ni-SiOC nanocomposites, NC Ni and coarse-grained Ni (inset) at different temperatures.

#### 4.2. Plastic co-deformation of Ni-SiOC nanocomposites

Deformation mechanisms of amorphous ceramic and Ni nanograins in Ni-SiOC nanocomposites were revealed based on micro-structure characterizations. For the core-shell nanostructures, i.e., the as-deposited and 400 °C annealed Ni-SiOC nanocomposites, they show similar deformation mechanism (Wei et al., 2021). Fig. 9 shows the deformed microstructure of as-deposited sample and Supplementary video V1 records the *in-situ* deformation behavior. Cross-section STEM image of deformed micropillar (Fig. 9a) shows high plastic flow stability without crack and shear instability though macroscale geometry instability happened at a certain compression strain corresponding to slightly softening in Figs. 5a and 6a. No strain induced coarsening of Ni nanograins was observed as evidenced by the enlarged TEM image and corresponding diffraction pattern (Fig. 9b). The size variation of Ni nanograins in the longitudinal and transversal directions indicates the shape change of Ni nanograins accomplished by dislocation motion (Fig. 9c). More importantly, amorphous SiOC boundaries act as strong barriers for preventing grain coarsening while co-deform with Ni nanograins to accommodate the shape change and rotation of Ni nanograins, achieving superb plastic flow stability.

Fig. 10 presents the RT deformed microstructure of 600 °C annealed Ni-SiOC nanocomposite. The corresponding *in situ* deformation is recorded in Supplementary video V2. The micropillar after compression test shows obvious shape change and no shear instability happened inside as shown in the cross-sectional STEM image (Fig. 10a), indicating high plastic flow stability. Fig. 10b shows a representative TEM bright field image. Clearly, both Ni nanograins and amorphous ceramic SiOC particles were compressed into stripes perpendicular to the loading direction. The comparison of aspect ratio for Ni and amorphous SiOC phase (longest direction divided by shortest direction) before and after deformation in Fig. 10c1-c2 show the clear deformation induced shape change. HRTEM observation (Fig. 10d, e) was further performed to elucidate the co-deformation mechanism of Ni-SiOC nanocomposites. Elongated amorphous bands connected with Ni nanograins were outlined by the yellow dashed lines in Fig. 10d, showing high plastic flow stability of amorphous ceramic SiOC. Due to the presence of both amorphous SiOC particles and the remained SiOC phase/segregation along grain boundaries, deformation induced grain coarsening was retarded. High density stacking faults of {111} plane was frequently observed in Ni nanograins as shown in Fig. 10e, implying that nucleation and emission of partial dislocations should be the

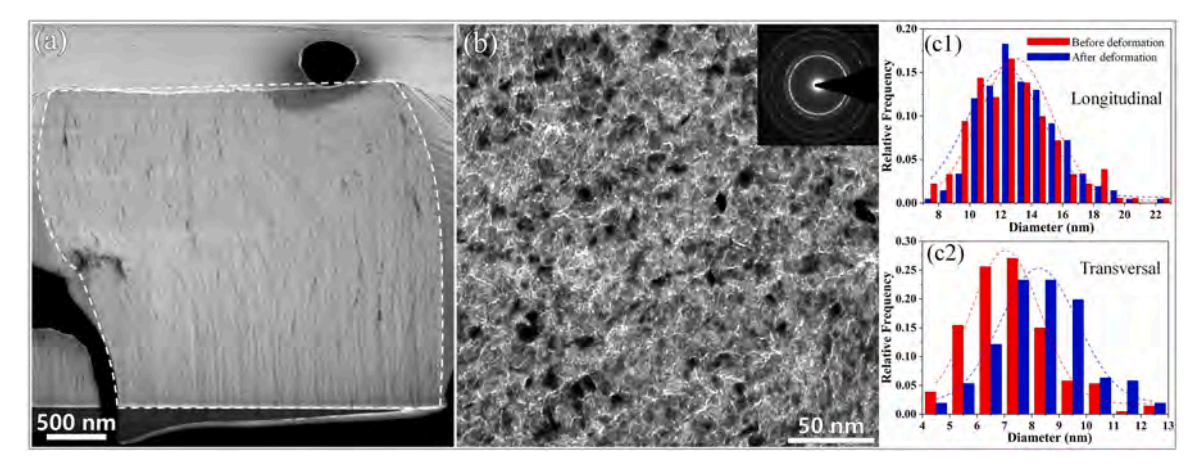


Fig. 9. Microstructure of the deformed as-deposited Ni-SiOC nanocomposite. (a) Cross-sectional STEM image of the compressed micropillar. (b) TEM bright field image and corresponding diffraction pattern in the deformed micropillar. (c1-c2) Size distribution of Ni nanograins along longitudinal and transversal directions before and after compression, respectively.

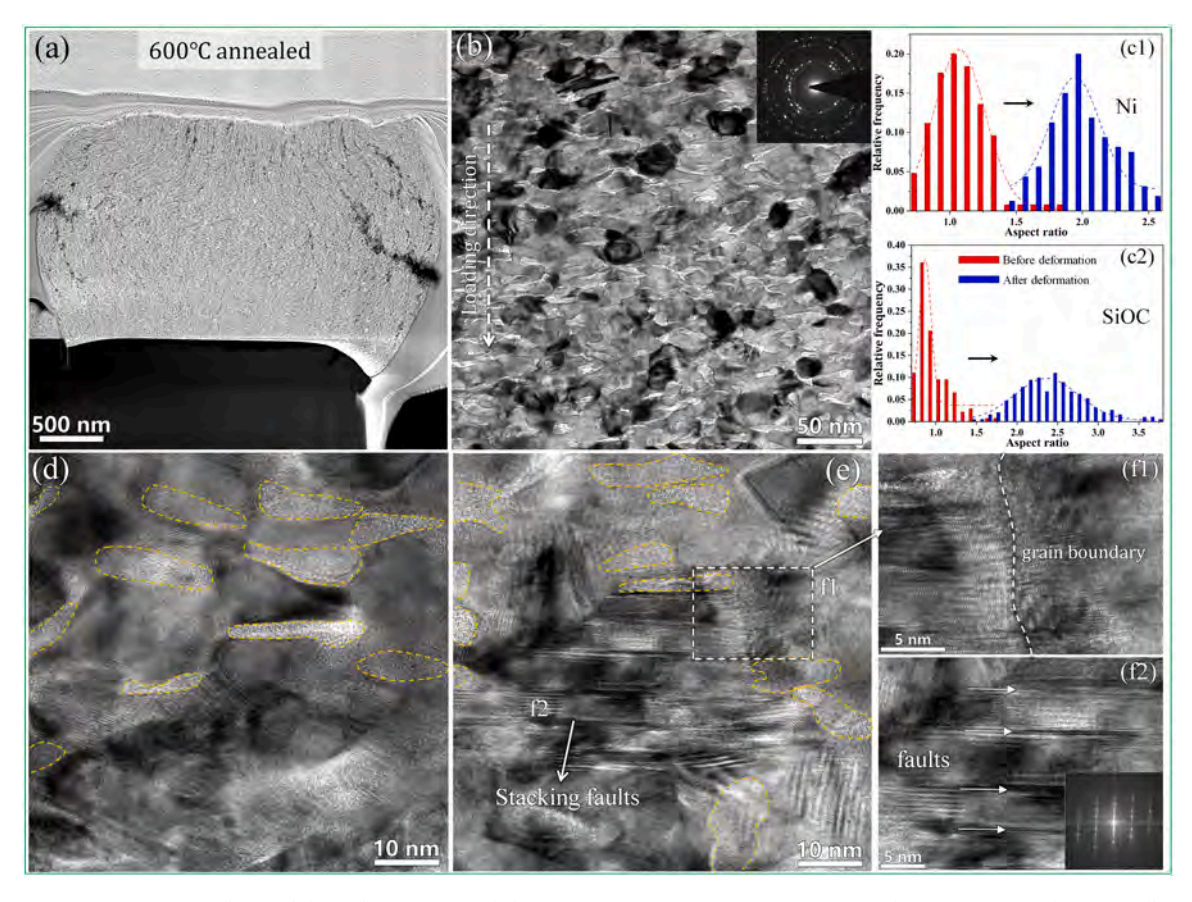


Fig. 10. Microstructures of the RT-deformed 600 °C annealed Ni-SiOC nanocomposite. (a) Cross-sectional STEM image of the micropillar after compression test; (b) Representative TEM bright field image and corresponding diffraction pattern of deformed micropillar; (c1-c2) Aspect ratio distribution of Ni and amorphous ceramic SiOC particles before and after compression, respectively; (d-f) HRTEM observation of microstructure after compression.

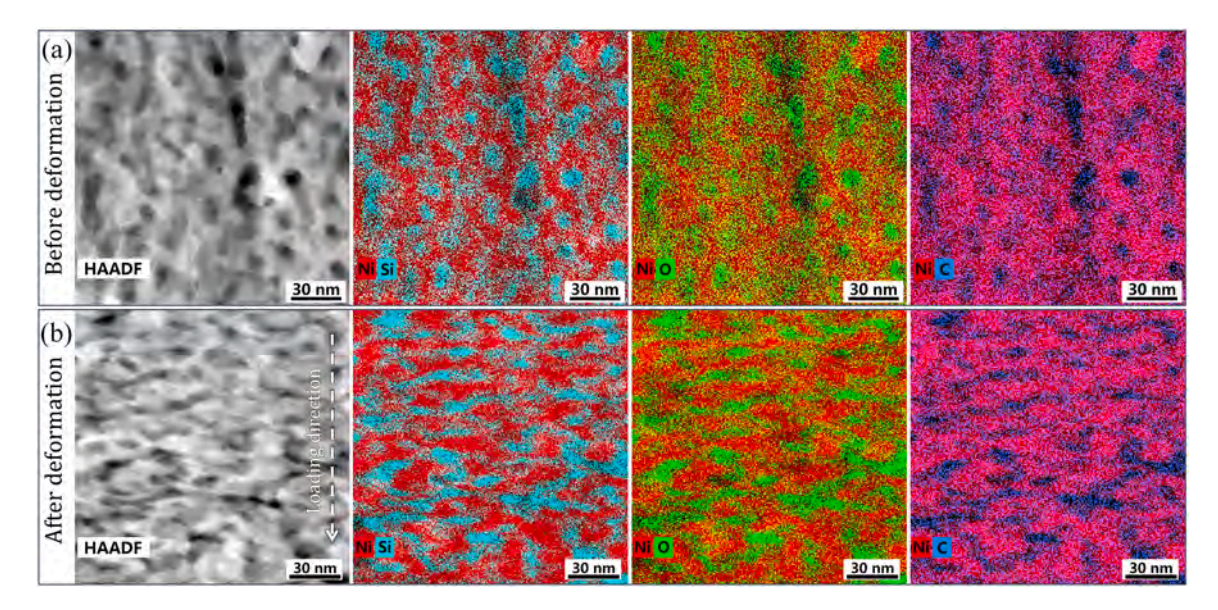


Fig. 11. (a-b) STEM-Mapping of 600 °C annealed Ni-SiOC nanocomposite before and after deformation, respectively.

dominant deformation mechanism in Ni nanograins. This is also supported by our SRJ tests (Fig. 7). Fig. 10f1 is the enlarged HRTEM image which show partial dislocations are terminated at grain boundary. Fig. 10f, 2 reveal the enlarged HRTEM image of NC Ni with high density of stacking faults and corresponding FFT pattern. The above results clearly indicate that the co-deformation between Ni nanograins and amorphous SiOC particles proceeds in 600 °C annealed Ni-SiOC nanocomposite, which was accomplished by partial dislocation slip in Ni nanograins and viscoplastic flow of amorphous ceramic SiOC. The co-deformation behavior was further verified by the comparison of STEM-Mappings before and after compression as presented in Fig. 11a, b. Due to the fine grain size and high velocity of dislocations at high stress, the interactions between partial dislocations and stacking faults rarely happened, corresponding to no obvious strain hardening behavior.

Fig. 12 presents deformed microstructure of 800 °C annealed sample. Cross-sectional SEM image of micropillar after deformation (Fig. 12a) shows no cracks and shear bands. Compared with the un-deformed domain of the micropillar, amorphous SiOC particles (dark contrast) exhibit shape change. Note that in contrast to the smooth surface of 600 °C annealed micropillar after deformation, Ni protrudes to form wrinkled surface (marked by pink arrows) in 800 °C annealed sample, implying deformation incompatibility between sub-micron sized Ni and amorphous SiOC ceramic particles. Fig. 12b is the corresponding TEM image of the deformed micropillar, clearly showing elongated SiOC particles in the deformed domain. To further verify the deformation induced shape change of SiOC particles, the aspect ratio distribution of SiOC particles (longest direction divided by shortest direction) before and after deformation were measured, respectively as shown in Fig. 12c. Due to the existence of obvious deformation incompatibility, local interface decohesion between Ni grains and amorphous SiOC particles was occasionally observed as indicated by yellow arrows in Fig. 12d. The contrast difference in Ni grains indicates the storage of dislocations. Fig. 12e shows a representative HRTEM image of Ni grain observed along <110> direction, in which a dislocation wall was observed, leading to a local misorientation of about 5° as evidenced by the inserted FFT pattern. High density dislocations were observed in the domain close to dislocation wall as presented in the Fourier filtered HRTEM image (Fig. 12f). It is worth mentioning that strain hardening should exist associated with the storage of dislocations in Ni grains, however, the stress-strain curve does not show obvious strain hardening behavior (Fig. 5a). This should be caused by the softening behavior associated with local interface decohesion. Despite of local interface decohesion, no crack nucleation/propagation and deformation instability were produced in micropillar during deformation. This should be attributed to high density of Ni-SiOC interfaces and co-deformation between Ni grains and amorphous SiOC particles, which effectively prevent strain localization and crack propagation.

Fig. 13 presents the SEM snapshots of 800 °C annealed Ni-SiOC micropillar with increasing strain, which clearly show plastic co-

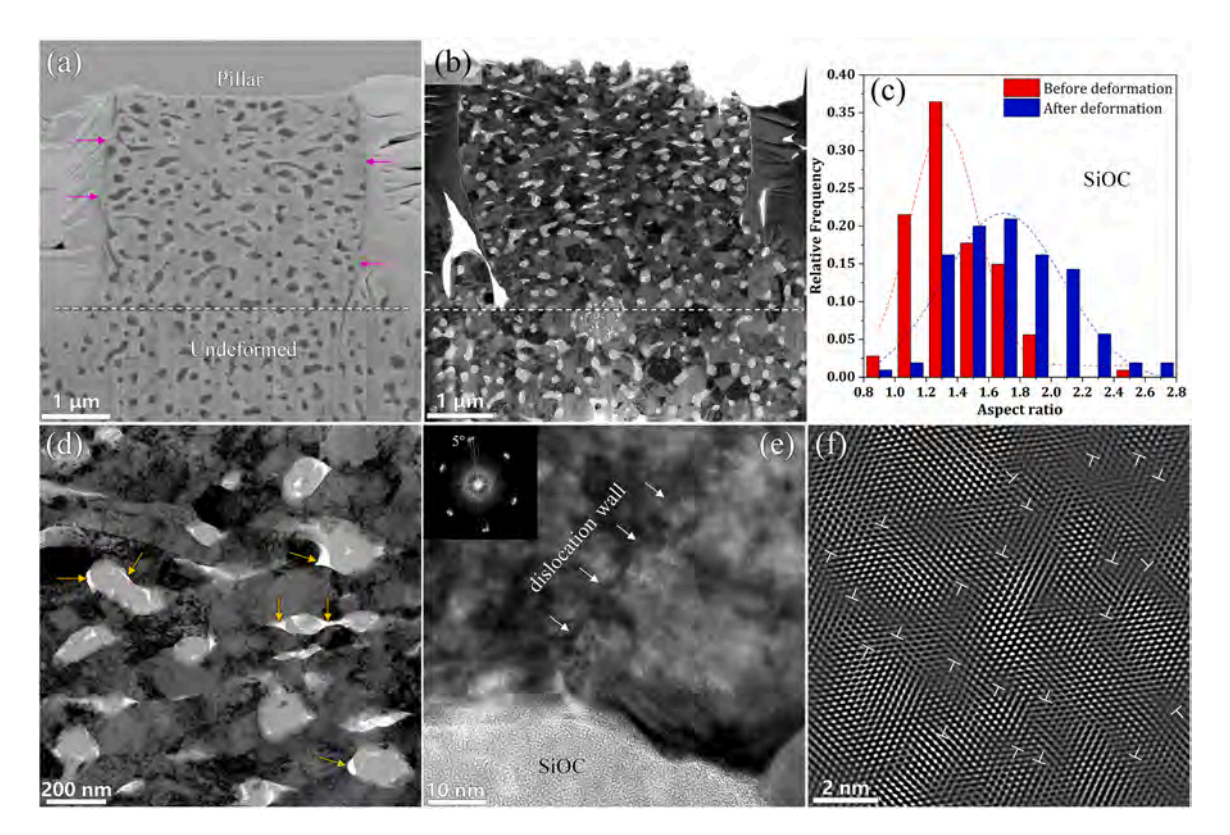


Fig. 12. Microstructures of the RT-deformed 800 °C annealed Ni-SiOC nanocomposite. (a) Cross-sectional SEM image of the micropillar after compression test; (b) Representative TEM bright field image of the deformed micropillar; (c) Aspect ratio distribution of amorphous ceramic SiOC particles before and after compression; (d) Enlarged TEM bright field image of the deformed micropillar; (e) and (f) HRTEM characterization of Ni after compression.

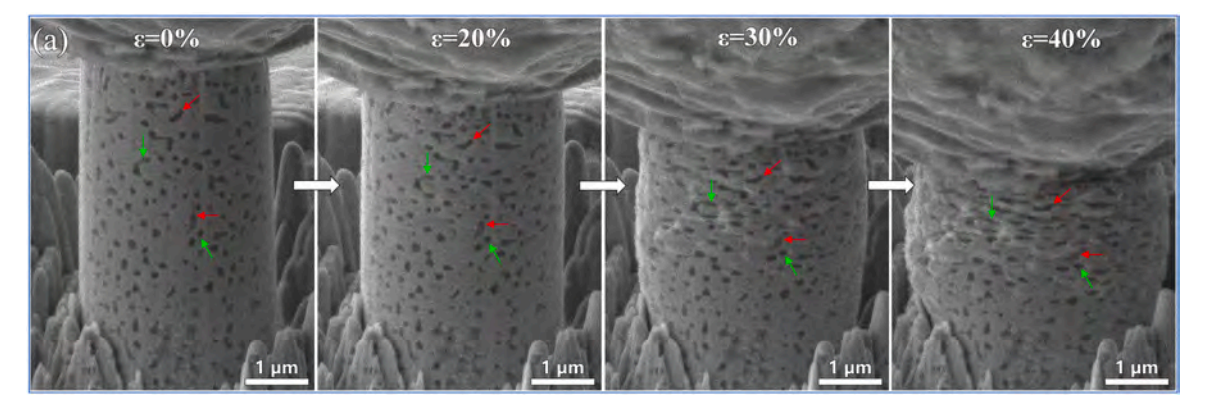


Fig. 13. SEM snapshots of the 800 °C annealed micropillar during compression.

deformation between Ni and amorphous SiOC particles, and the corresponding *in-situ* deformation is recorded in Supplementary video V3. Two types of deformation modes were identified with amorphous SiOC particles: i) direct plastic flow (marked by green arrows) and ii) rotation coupled with plastic flow (marked by red arrows). STEM images before and after deformation in Fig. 14 show plastic deformation induced shape change of both Ni grains and amorphous SiOC particles. It is noted that the co-deformation extent of the large SiOC particles in 800 °C annealed sample is limited compared to that in 600 °C annealed sample where amorphous SiOC particles are stretched along with Ni grains (Fig. 10).

#### 4.3. Microstructure/composition dependent mechanical behavior

Microstructure evolution in Ni-SiOC nanocomposites indicates that Ni and amorphous SiOC tend to separate from each other during high temperature annealing. Thus, we can speculate that the content of Ni element in amorphous SiOC decreases with high temperature annealing. Recently, we have demonstrated that increasing the content of Fe element in amorphous SiOC will reduce the flow strength of amorphous SiOC while increase its plasticity (Ming et al., 2020). Since Ni and Fe have the similar electronegativity to Si, O, and C elements (Luo, 2007), the flow strength of amorphous SiOC would increase due to the reduced Ni content during high temperature annealing. The improved mechanical property of Ni-SiOC nanocomposite after 600 °C annealing can thus be ascribed by the following reasons. First, the slightly increased grain size of Ni grains from 13 nm to 20 nm after 600 °C annealing will not extensively decrease the flow strength of Ni-SiOC nanocomposite. Moreover, the inserted amorphous SiOC particles in Ni grains also act as strong barriers for dislocation motion. Second, the flow strength of amorphous SiOC ceramic increases after annealing due to the reduced Ni content, which contributes to enhanced strength of 600 °C annealed Ni-SiOC nanocomposite. Third, the amorphous SiOC particles in the 600 °C annealed sample plastically co-deformed with Ni nanograins due to the enhanced flow strength of Ni-SiOC nanocomposites. Compared to the 600 °C annealed Ni-SiOC nanocomposite, the 800 °C annealed sample exhibited a decreased flow strength although amorphous SiOC might become much stronger due to the further reduced content of Ni in amorphous SiOC. The strength decrease is mainly ascribed to obvious growth of Ni grains according to the Hall-Petch relationship. Corresponding to the decrease in the flow strength of Ni-SiOC nanocomposite and the increase in the flow strength of amorphous SiOC, the incompatibility of plastic deformation between amorphous SiOC and Ni nanograins will develop with deformation extend, leading to interface decohesion between Ni and amorphous SiOC particles. To retain a good plastic flow stability, the present results suggests that it is worth studying the strength effect of amorphous ceramics via adjusting the content of metal elements.

## 5. Conclusion

Corresponding to a large volume fraction of boundaries and nanosized constituents, mechanical behavior and properties of nanocomposites are dominated by their characteristic microstructure and corresponding deformation processes related to boundaries, characteristic size and properties of nanosized constituents. Thus, strength, plasticity and thermal stability that are highly desired for structural materials could be realized through optimizing their microstructure. We demonstrated this in crystal-amorphous ceramics Ni-SiOC nanocomposites. The following conclusions are drawn:

- (1) Two characteristic microstructures of crystal-amorphous ceramics Ni-SiOC nanocomposites were developed by co-sputtering and high temperature annealing: i) core-shell nanostructures in as-deposited and 400 °C annealed samples and ii) nanograined Ni containing nanosized amorphous ceramic SiOC particles in high temperature annealed samples.
- (2) *In-situ* micropillar compression tests revealed that Ni-SiOC nanocomposites exhibit high strength and large deformability. The core-shell nanostructure shows high strength of 2.5 GPa at RT and 1.6 GPa at 400 °C with compressive strain up to 40%, the 600 °C annealed Ni nanograins containing amorphous ceramic nanoparticles exhibits high strength of 3 GPa at RT and 2 GPa at 400 °C with compressive strain up to 50%, and the 800 °C annealed Ni nanograins containing amorphous ceramic nanoparticles exhibits high strength of 1.5 GPa at RT with compressive strain up to 40%.

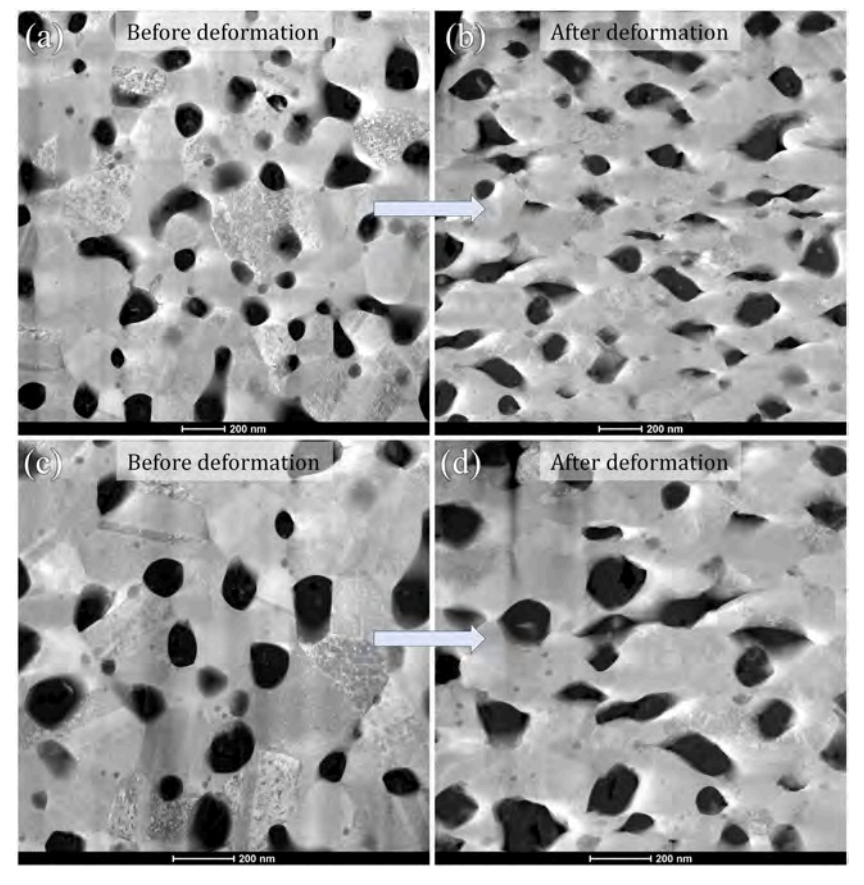


Fig. 14. STEM images of the 800 °C annealed Ni-SiOC nanocomposite (a, c) before and (b, d) after deformation.

- (3) *In-situ* mechanical tests and microstructural characterization after deformation indicates that the amorphous SiOC ceramic impart high strength, good thermal stability and large deformability to Ni-SiOC nanocomposites. More importantly, amorphous SiOC ceramic co-deformed with Ni, contributing to superb plastic flow stability.
- (4) SRJ tests suggest that plastic deformation is accommodated by dislocation slip in Ni grains, which is further verified in HRTEM images. For the core-shell nanostructures and 600 °C annealed Ni-SiOC nanocomposite, amorphous ceramic SiOC boundaries and nanoparticles deform visco-plastically along with Ni nanograins. Corresponding to the large size of amorphous SiOC nanoparticles in the 800 °C annealed Ni-SiOC nanocomposite, amorphous ceramic SiOC nanoparticles deform via two modes, viscoplastic flow and rotation coupled with viscoplastic flow. Deformation incompatibility between Ni and amorphous SiOC particles develops with straining in 800 °C annealed nanocomposite and results in interface decohesion.
- (5) A synergetic improvement of strength and plasticity in crystal-amorphous ceramics nanocomposites could be achieved by further improving deformation compatibility via tailoring characteristic dimensions and mechanical properties of amorphous ceramics.

#### Author statement

Wei and Wu synthesized materials and performed *in situ* micro-mechanical tests and TEM characterization; Wei, Wu and Wang prepared the manuscript. Nastasi, Li and Wang conceived this study. All authors commented the manuscript.

## **Declaration of Competing Interest**

The authors declare that they have no known competing financial interests or personal relationships that could have appeared to influence the work reported in this paper.

## Data availability

Data will be made available on request.

#### Acknowledgments

The research was financially supported by the US National Science Foundation (NSF) (CMMI- 2132336/2132383), and performed in the Nebraska Center for Materials and Nanoscience which is supported by the National Science Foundation under Award ECCS: 1542182 and the Nebraska Research Initiative.

#### Supplementary materials

Supplementary material associated with this article can be found, in the online version, at doi:10.1016/j.ijplas.2022.103431.

#### References

- Abdolrahim, N., Bahr, D.F., Revard, B., Reilly, C., Ye, J., Balk, T.J., Zbib, H.M., 2013. The mechanical response of core-shell structures for nanoporous metallic materials. Philos. Mag. 93, 736–748.
- Barai, P., Weng, G.J., 2009. Mechanics of very fine-grained nanocrystalline materials with contributions from grain interior, GB zone, and grain-boundary sliding. Int. J. Plast. 25, 2410–2434.
- Beyerlein, I.J., Caro, A., Demkowicz, M.J., Mara, N.A., Misra, A., Uberuaga, B.P., 2013. Radiation damage tolerant nanomaterials. Mater. Today 16, 443–449. Brandstetter, S., Budrović, Ž., Petegem, S.V., Schmitt, B., Stergar, E., Derlet, P.M., Swygenhoven, H.V., 2005. Temperature-dependent residual broadening of x-ray diffraction spectra in nanocrystalline plasticity. Appl. Phys. Lett. 87, 231910.
- Cao, Y., Zhang, W., Liu, B., Liu, Y., Du, M., Fu, A., 2021. Phase decomposition behavior and its effects on mechanical properties of TiNbTa0.5ZrAl0.5 refractory high entropy alloy. J. Mater. Sci. Technol. 66, 10–20.
- Chen, H.H., Zhao, Y.F., Zhang, J.Y., Wang, Y.Q., Li, G.Y., Wu, K., Liu, G., Sun, J., 2020. He-ion irradiation effects on the microstructure stability and size-dependent mechanical behavior of high entropy alloy/Cu nanotwinned nanolaminates. Int. J. Plast. 133, 102839.
- Cheng, S., Spencer, J.A., Milligan, W.W., 2003. Strength and tension/compression asymmetry in nanostructured and ultrafine-grain metals. Acta Mater. 51, 4505–4518.
- Chyrkin, A., Pillai, R., Ackermann, H., Hattendorf, H., Richter, S., Nowak, W., Grüner, D., Quadakkers, W.J., 2015. Modeling carbide dissolution in alloy 602 CA during high temperature oxidation. Corros. Sci. 96, 32–41.
- Cottrell, A.H., Stokes, R.J., 1955. Effects of temperature on the plastic properties of aluminium crystals. Proc. R. Soc. Lond. Ser. A. Math. Phys. Sci. 233, 17–34. Cui, Y., Abad, O.T., Wang, F., Huang, P., Lu, T.-J., Xu, K.-W., Wang, J., 2016. Plastic deformation modes of CuZr/Cu multilayers. Sci. Rep. 6, 23306.
- Dalla Torre, F., Spätig, P., Schäublin, R., Victoria, M., 2005. Deformation behaviour and microstructure of nanocrystalline electrodeposited and high pressure torsioned nickel. Acta Mater 53, 2337–2349.
- Ebrahimi, F., Bourne, G.R., Kelly, M.S., Matthews, T.E., 1999. Mechanical properties of nanocrystalline nickel produced by electrodeposition. Nanostruct. Mater. 11, 343–350.
- Fan, L., Yang, T., Zhao, Y., Luan, J., Zhou, G., Wang, H., Jiao, Z., Liu, C.-T., 2020. Ultrahigh strength and ductility in newly developed materials with coherent nanolamellar architectures. Nat. Commun. 11, 6240.
- Freund, L.P., Stark, A., Pyczak, F., Schell, N., Göken, M., Neumeier, S., 2018. The grain boundary pinning effect of the  $\mu$  phase in an advanced polycrystalline  $\gamma/\gamma'$  Cobase superalloy. J. Alloy. Compd. 753, 333–342.
- Grant, B.M.B., Francis, E.M., Quinta da Fonseca, J., Daymond, M.R., Preuss, M., 2012. Deformation behaviour of an advanced nickel-based superalloy studied by neutron diffraction and electron microscopy. Acta Mater. 60, 6829–6841.
- Grigorian, C.M., Rupert, T.J., 2019. Thick amorphous complexion formation and extreme thermal stability in ternary nanocrystalline Cu-Zr-Hf alloys. Acta Mater 179, 172–182
- Guo, H., Yan, P.F., Wang, Y.B., Tan, J., Zhang, Z.F., Sui, M.L., Ma, E., 2007. Tensile ductility and necking of metallic glass. Nat. Mater. 6, 735-739.
- Guo, W., Jägle, E., Yao, J., Maier, V., Korte-Kerzel, S., Schneider, J.M., Raabe, D., 2014. Intrinsic and extrinsic size effects in the deformation of amorphous CuZr/nanocrystalline Cu nanolaminates. Acta Mater. 80, 94–106.
- Han, L., Rao, Z., Souza Filho, I.R., Maccari, F., Wei, Y., Wu, G., Ahmadian, A., Zhou, X., Gutfleisch, O., Ponge, D., Raabe, D., Li, Z., 2021. Ultrastrong and ductile soft magnetic high-entropy alloys via coherent ordered nanoprecipitates. Adv. Mater. 33, 2102139.
- Hasan, M.N., Liu, Y.F., An, X.H., Gu, J., Song, M., Cao, Y., Li, Y.S., Zhu, Y.T., Liao, X.Z., 2019. Simultaneously enhancing strength and ductility of a high-entropy alloy via gradient hierarchical microstructures. Int. J. Plast. 123, 178–195.
- He, J.Y., Wang, H., Huang, H.L., Xu, X.D., Chen, M.W., Wu, Y., Liu, X.J., Nieh, T.G., An, K., Lu, Z.P., 2016. A precipitation-hardened high-entropy alloy with outstanding tensile properties. Acta Mater. 102, 187–196.
- Hirth, J.P., 1972. The influence of grain boundaries on mechanical properties. Metall. Trans. 3, 3047–3067.
- Jang, D., Greer, J.R., 2010. Transition from a strong-yet-brittle to a stronger-and-ductile state by size reduction of metallic glasses. Nat. Mater. 9, 215–219.
- Jiang, H., Dong, J., Zhang, M., 2019. The phase decomposition with related element interaction and redistribution during long term aging of 740H superalloy. J. Alloy. Compd. 782, 323–333.
- Jiang, L., Yinling, W., Hu, R., Liu, R., Ye, X.-X., Li, Z., Zhou, X., 2018. Formation of nano-sized M2C carbides in Si-free GH3535 alloy. Sci. Rep. 8, 8158.
- Kim, S.-H., Kim, H., Kim, N.J., 2015. Brittle intermetallic compound makes ultrastrong low-density steel with large ductility. Nature 518, 77–79.
- Lee, S.-W., Han, S.M., Nix, W.D., 2009. Uniaxial compression of fcc Au nanopillars on an MgO substrate: the effects of prestraining and annealing. Acta Mater. 57, 4404–4415.
- Liao, Y., 2006. Practical Electron Microscopy and Database. An Online Book.
- Lieou, C.K.C., Mayeur, J.R., Beyerlein, I.J., 2017. Deformation in amorphous–crystalline nanolaminates—an effective-temperature theory and interaction between defects. Model. Simul. Mater. Sci. Eng. 25, 034002.
- Liu, W.B., Zhang, C., Ji, Y.Z., Yang, Z.G., Zang, H., Shen, T.L., Chen, L.Q., 2014. Irradiation-induced grain growth in nanocrystalline reduced activation ferrite/martensite steel. Appl. Phys. Lett. 105, 121905.
- Liu, Y., Kang, M., Wu, Y., Wang, M., Li, M., Yu, J., Gao, H., Wang, J., 2018a. Crack formation and microstructure-sensitive propagation in low cycle fatigue of a polycrystalline nickel-based superalloy with different heat treatments. Int. J. Fatigue 108, 79–89.
- Liu, Y.Y., Liu, P.Z., Li, J.J., Liaw, P.K., Spieckermann, F., Kiener, D., Qiao, J.W., Eckert, J., 2018b. Universally scaling Hall-Petch-like relationship in metallic glass matrix composites. Int. J. Plast. 105, 225–238.
- Long, H., Mao, S., Liu, Y., Zhang, Z., Han, X., 2018. Microstructural and compositional design of Ni-based single crystalline superalloys a review. J. Alloy. Compd. 743, 203–220.
- Lu, K., 2016. Stabilizing nanostructures in metals using grain and twin boundary architectures. Nat. Rev. Mater. 1, 16019.
- Luo, Y.-R., 2007. Comprehensive Handbook of Chemical bond Energies. CRC press.
- Ma, Z., Samuel, A.M., Doty, H.W., Samuel, F.H., 2016. On the fractography of impact-tested samples of Al-Si alloys for automotive alloys. Fracture Mechanics—Properties, Patterns and Behaviours.

- Meyers, M.A., Mishra, A., Benson, D.J., 2006. Mechanical properties of nanocrystalline materials. Prog. Mater. Sci. 51, 427-556.
- Ming, K., Gu, C., Su, Q., Xie, D., Wu, Y., Wang, Y., Shao, L., Nastasi, M., Wang, J., 2020. Strength and plasticity of amorphous ceramics with self-patterned nanoheterogeneities. Int. J. Plast. 134. 102837.
- Ming, K., Zhu, Z., Zhu, W., Fang, B., Wei, B., Liaw, P.K., Wei, X., Wang, J., Zheng, S., 2022. Enhancing strength and ductility via crystalline-amorphous nanoarchitectures in TiZr-based alloys. Sci. Adv. 8. eahm2884
- Ning, Y., Yao, Z., Guo, H., Fu, M.W., 2013. Structural-gradient-materials produced by gradient temperature heat treatment for dual-property turbine disc. J. Alloy. Compd. 557, 27–33.
- Oliver, W.C., Pharr, G.M., 1992. An improved technique for determining hardness and elastic modulus using load and displacement sensing indentation experiments. J. Mater. Res. 7, 1564–1583.
- Pan, D., Kuwano, S., Fujita, T., Chen, M.W., 2007. Ultra-large room-temperature compressive plasticity of a nanocrystalline metal. Nano Lett. 7, 2108–2111.
- Qiao, J., Jia, H., Liaw, P.K., 2016. Metallic glass matrix composites. Mater. Sci. Eng. R Rep. 100, 1-69.
- Reed, R.C., 2008. The Superalloys: Fundamentals and Applications. Cambridge University Press.
- Schuh, C.A., Nieh, T.G., Iwasaki, H., 2003. The effect of solid solution W additions on the mechanical properties of nanocrystalline Ni. Acta Mater. 51, 431-443.
- Schuh, C.A., Nieh, T.G., Yamasaki, T., 2002. Hall-Petch breakdown manifested in abrasive wear resistance of nanocrystalline nickel. Scr. Mater. 46, 735–740.
- Schuler, J.D., Grigorian, C.M., Barr, C.M., Boyce, B.L., Hattar, K., Rupert, T.J., 2020. Amorphous intergranular films mitigate radiation damage in nanocrystalline Cu-Zr. Acta Mater. 186, 341–354.
- Sharma, G., Chatterjee, A., Paul, B., Varshney, J., Chakravartty, J.K., 2013. High temperature mechanical behavior of nanocrystalline Ni. Mater. Sci. Eng., A 576, 69–73.
- Sharma, G., Varshney, J., Bidaye, A.C., Chakravartty, J.K., 2012. Grain growth characteristics and its effect on deformation behavior in nanocrystalline Ni. Mater. Sci. Eng., A 539, 324–329.
- Sheinerman, A.G., Bobylev, S.V., 2018. A model of enhanced strain rate sensitivity in nanocrystalline and ultrafine-grained metals. Rev. Adv. Mater. Sci. 57, 1–10. Shi, R., Fu, H., Chen, K., Sun, W., Wang, Z., Qiao, L., Yang, X.-S., Pang, X., 2022. Combining synergetic effects of gradient nanotwins and nanoprecipitates in heterogeneous bronze alloy. Acta Mater. 229, 117831.
- Sneddon, I.N., 1965. The relation between load and penetration in the axisymmetric boussinesq problem for a punch of arbitrary profile. Int. J. Eng. Sci. 3, 47–57. Su, Q., Inoue, S., Ishimaru, M., Gigax, J., Wang, T., Ding, H., Demkowicz, M.J., Shao, L., Nastasi, M., 2017. Helium irradiation and implantation effects on the structure of amorphous silicon oxycarbide. Sci. Rep. 7, 3900.
- Su, Q., Wang, T., Gigax, J., Shao, L., Nastasi, M., 2019. Resistance to helium bubble formation in amorphous SiOC/Crystalline Fe nanocomposite. Materials 12. Tang, Y., Zhou, H., Lu, H., Wang, X., Cao, Q., Zhang, D., Yang, W., Jiang, J.-Z., 2022. Extra plasticity governed by shear band deflection in gradient metallic glasses. Nat. Commun. 13, 2120.
- Tran, A.-S., 2021. Strengthening mechanism and plasticity deformation of crystalline/amorphous Cu/CuTa nanomultilayer. J. Non-Cryst. Solids 559, 120685. Wang, C., Luo, K., Wang, J., Lu, J., 2022. Carbide-facilitated nanocrystallization of martensitic laths and carbide deformation in AISI 420 stainless steel during laser shock peening. Int. J. Plast. 150, 103191.
- Wang, J., Zhou, Q., Shao, S., Misra, A., 2017. Strength and plasticity of nanolaminated materials. Mater. Res. Lett. 5, 1-19.
- Wang, Y., Li, J., Hamza, A.V., Barbee, T.W., 2007. Ductile crystalline-amorphous nanolaminates. Proc. Natl. Acad. Sci. 104, 11155–11160.
- Wang, Y., Pan, Z., Ho, Y., Xu, Y., Du, A., 2001. Nuclear instruments and methods in physics research section B: beam interactions with materials and atoms. Nucl. Instrum. Methods Phys. Res. B 180, 251–256.
- Wang, Y.M., Hamza, A.V., Ma, E., 2006. Temperature-dependent strain rate sensitivity and activation volume of nanocrystalline Ni. Acta Mater. 54, 2715–2726. Wang, Y.M., Ma, E., 2004. On the origin of ultrahigh cryogenic strength of nanocrystalline metals. Appl. Phys. Lett. 85, 2750–2752.
- Wang, Y.M., Ott, R.T., Besser, M.F., Hamza, A.V., 2012. Temperature-dependent competing deformation mechanisms in nanocrystalline metals. Phys. Rev. B 85, 144122
- Wang, Z., Lu, W., Zhao, H., Liebscher, C.H., He, J., Ponge, D., Raabe, D., Li, Z., 2020. Ultrastrong lightweight compositionally complex steels via dual-nanoprecipitation. Sci. Adv. 6, eaba9543.
- Wei, B., Wu, W., Xie, D., Nastasi, M., Wang, J., 2021. Strength, plasticity, thermal stability and strain rate sensitivity of nanograined nickel with amorphous ceramic grain boundaries. Acta Mater. 212, 116918.
- Wu, G., Liu, C., Sun, L., Wang, Q., Sun, B., Han, B., Kai, J.-J., Luan, J., Liu, C.T., Cao, K., Lu, Y., Cheng, L., Lu, J., 2019. Hierarchical nanostructured aluminum alloy with ultrahigh strength and large plasticity. Nat. Commun. 10, 5099.
- Xiang, X., Yao, Z., Dong, J., Sun, L., 2019. Dissolution behavior of intragranular M23C6 carbide in 617B Ni-base superalloy during long-term aging. J. Alloy. Compd. 787, 216–228.
- Xiao, X., Song, D., Chu, H., Xue, J., Duan, H., 2015. Mechanical behaviors of irradiated FCC polycrystals with nanotwins. Int. J. Plast. 74, 110-126.
- Yuan, F., Yan, D., Sun, J., Zhou, L., Zhu, Y., Wu, X., 2019. Ductility by shear band delocalization in the nano-layer of gradient structure. Mater. Res. Lett. 7, 12–17. Zhang, H.W., Lu, K., Pippan, R., Huang, X., Hansen, N., 2011. Enhancement of strength and stability of nanostructured Ni by small amounts of solutes. Scr. Mater. 65, 481–484.
- Zhang, J.Y., Liu, G., Lei, S.Y., Niu, J.J., Sun, J., 2012. Transition from homogeneous-like to shear-band deformation in nanolayered crystalline Cu/amorphous Cu–Zr micropillars: intrinsic vs. extrinsic size effect. Acta Mater. 60, 7183–7196.
- Zhang, X., Hattar, K., Chen, Y., Shao, L., Li, J., Sun, C., Yu, K., Li, N., Taheri, M.L., Wang, H., Wang, J., Nastasi, M., 2018. Radiation damage in nanostructured materials. Prog. Mater. Sci. 96, 217–321.
- Zhang, Y., Tucker, G.J., Trelewicz, J.R., 2017. Stress-assisted grain growth in nanocrystalline metals: Grain boundary mediated mechanisms and stabilization through alloying. Acta Mater. 131, 39–47.
- Zhao, Z., Niu, M., Wang, H., Gao, H., Peng, K., Zang, H., Ma, M., 2019. Preparation and the effects of ion irradiation on bulk SiOC ceramics. J. Eur. Ceram. Soc. 39, 832–837.
- Zhou, H., Qu, S., Yang, W., 2013. An atomistic investigation of structural evolution in metallic glass matrix composites. Int. J. Plast. 44, 147-160.
- Zhu, Y., Ameyama, K., Anderson, P.M., Beyerlein, I.J., Gao, H., Kim, H.S., Lavernia, E., Mathaudhu, S., Mughrabi, H., Ritchie, R.O., Tsuji, N., Zhang, X., Wu, X., 2021. Heterostructured materials: superior properties from hetero-zone interaction. Mater. Res. Lett. 9, 1–31.